



Structural and morphological analysis of rf sputtered nano ZnSe coatings as a function of thickness: investigation of the effect of metal contact on MIS structure with ZnSe interfacial layer

Esra Balcı^{1,*} , Barış Kınacı^{2,3}, Çağlar Çetinkaya⁴, Erman Çokduygulular⁵, Tuğçe Ataşer^{2,3}, Nihan Akın Sönmez^{2,3}, Semran Sağlam⁶, and Süleyman Özçelik^{2,3}

¹Polatlı Science and Literature Faculty, Physics Department, Ankara Hacı Bayram Veli University, Ankara, Turkey

²Department of Photonics, Faculty of Applied Sciences, Gazi University, 06500 Ankara, Turkey

³Photonics Application and Research Center, Gazi University, 06500 Ankara, Turkey

⁴Physics Department, Faculty of Science, Istanbul University, 34134 Istanbul, Turkey

⁵Department of Engineering Sciences, Faculty of Engineering, Istanbul University-Cerrahpaşa, 34320 Istanbul, Turkey

⁶Physics Department, Faculty of Science, Gazi University, 06500 Ankara, Turkey

Received: 23 December 2022

Accepted: 21 May 2023

Published online:

6 June 2023

© The Author(s), under exclusive licence to Springer Science+Business Media, LLC, part of Springer Nature 2023

ABSTRACT

In this study, to examine the effect of the thickness difference on the physical properties, ZnSe thin films with three different thicknesses were deposited by the RF sputter technique on Si substrates. Measurements were carried out in XRD and AFM systems to determine the effect of films thickness deposited at 100, 300, and 600 nm on physical properties. It was observed that the crystallinity increased, and the surface roughness decreased with the increase in thickness. 600 nm thick ZnSe thin film was chosen for both XPS analysis and fabrication of Schottky diodes due to its high crystallinity and large grain size. XPS analysis was performed for the determination of the binding energy and elemental analysis on ZnSe. In addition, the effect of different metal contacts on the performance of MIS structures formed with a 600 nm thick ZnSe thin film interfacial layer produced using Au, Ag and Al metals was investigated in detail. Therefore, I–V measurements were performed to examine the electrical properties with Au/ZnSe/Si, Ag/ZnSe/Si ve Al/ZnSe/Si MIS structures. The Schottky diodes' performances were compared with each other by Thermionic Emission Theory, Cheung I–II, and Norde functions methods. Results show that Au/ZnSe/Si MIS structure performed better than the others.

Address correspondence to E-mail: balci.esra@hbv.edu.tr

1 Introduction

Zinc Selenide (ZnSe) is a solid semiconductor formed by combining the group II element Zn and the group VI element Se [1]. Binary compounds containing Zinc (Zn) offer a wide band gap, low absorption properties, and high optical transmittance in the visible region, making ZnSe a promising material for optoelectronic device applications [2, 3]. ZnSe has a large optical band gap of 2.7 eV [4, 5], high refractive index value, high transparency in the visible province, and a large exciton binding energy of 22 meV, providing unique electrical and optical properties. Due to its high sensitivity in various device applications in the visible and ultraviolet regions of the solar spectrum, ZnSe has attracted increasing interest [3]. ZnSe thin films have shown great potential for use in light emitting diodes [6], dielectric mirrors [7], sensors [8], photodiodes [9], photoluminescence, photodetectors, and lasers [10]. Various deposition techniques, including physical and chemical methods, have been used to grow ZnSe thin films on different substrates [3, 11]. Radio Frequency (RF) Magnetron Sputtering [12], Chemical Vapor Deposition (CVD) [13], Molecular Beam Epitaxy (MBE) [14], Electron Beam Evaporation [15], thermal Evaporation technique [16], and Sol-Gel Process [17] are some of the methods used for this purpose. The sputtering technique has proven to be effective in ensuring high-quality, uniform, and controllable film thickness [18–21]. Therefore, this study focuses on the deposition of ZnSe thin films using RF Magnetron Sputtering [22, 23].

Si-based technologies have a wide usage area for today's device applications since it is cheaper and contains known technology, and Si is used as a substrate or active layer in many electro-optic device configurations [24–33]. Among these technologies, Metal–semiconductor (MS) structures [24–26] formed by making metal contact with Si substrate, metal–interface layer–semiconductor (MIS/MOS) structures [27–33] formed by placing an interface layer between Si substrate and metal contact have an important place. Therefore, important device indicators such as device performance, quality, and sustainability can be evaluated by performing electrical analyzes of MS and MIS/MOS structures. Among these electrical analyzes, the fundamental electrical parameters of the structure, such as ideality factor, barrier height, and series resistance, can be determined by performing current–voltage analysis of MS and MIS/

MOS structures. Thus, whether the relevant structure is suitable for device applications is indicated.

ZnSe thin films with low film thicknesses have a narrow band gap and can be used in various applications, including lasers, optical switches, dielectric mirrors, and high electron mobility transistors (HEMTs). The narrow band gap of thin films with low film thickness makes them suitable for applications that require high-energy photon absorption, such as in solar cells and photodetectors. On the other hand, ZnSe thin films with high film thicknesses can be used in optoelectronic devices due to their superior structural and morphological properties. These thin films exhibit excellent crystallinity and morphological uniformity, making them ideal for applications requiring high-quality thin films. Moreover, thin films with high film thicknesses have a wider bandgap, making them suitable for applications where low absorption of high-energy photons is required, such as in infrared photodetectors. Zinc selenide (ZnSe) thin films have gained significant attention due to their potential applications in optoelectronics, solar cells, and photoelectrochemical devices. There are some publications in the literature on research on ZnSe [1, 34]. Abu et al. [1] performed structural optical and electrical characterizations of the ZnSe thin films they grew for different film thicknesses between 30 and 90 nm. In our study, unlike this, we varied the film thicknesses between 100 and 600 nm. It was aimed to observe the differences or similarities in the data obtained in the characterizations of the thickness difference. Hassaneen et al. [34] coated ZnSe thin films with different thicknesses between 200 and 650 nm by thermal evaporation technique. The structural, morphological and optic characterizations of the films show that increasing the film thickness leads to an increase in the crystalline quality and energy band gap, similar to the results obtained in our study. In addition, we took this study one step further and investigated the device with electrical characterization. In the present study, we investigated the effect of film thickness on the structural and morphological properties of ZnSe thin films deposited on silicon substrates using radio frequency (RF) sputtering at room temperature. Three different ZnSe thin films with thicknesses of 100 nm, 300 nm, and 600 nm were deposited using RF sputtering, and their structural and morphological properties were characterized using various techniques. The results showed that the particle size and

root mean square values of the 600 nm thick ZnSe thin film were higher than the other samples, and the Full Width Half Maximum value was lower than the other samples. Therefore, the focus is on electrical analysis for the ZnSe thin film structure with a thickness of 600 nm. Schottky Barrier Diodes (SBDs) were fabricated on the ZnSe thin film with a thickness of 600 nm using different metal contacts, including Au, Ag, and Al. The I–V characteristics of the SBDs were investigated, and the basic electrical parameters were determined using three different methods: thermionic emission (TE), Cheung I–II, and Norde methods. The results showed that the SBD formed with an Au contact outperformed the others due to its low ideality factor and low series resistance values. The study highlights the importance of film thickness on the structural and morphological properties of ZnSe thin films and the performance of SBDs fabricated on them. The results provide useful insights for developing ZnSe-based optoelectronic devices and pave the way for future research in this area.

2 Experimental

2.1 Preparation of ZnSe thin films

Si substrates were used for ZnSe thin film coating and fabrication processes. Before deposition, substrates were cleaned with acetone and isopropanol using an ultrasonic bath for 10 min to remove undesired particles. Then, it dried using nitrogen gas (N₂). Sputtered ZnSe thin films were deposited with different thicknesses by Radio Frequency Magnetron (RF) sputtering technique (Nanovak NVT5-500) using ZnSe (2 Inch and 99.99% purity) target. Deposition time is the significant parameter in obtaining ZnSe films with different thicknesses varying from 100 to 600 nm. During the implementation, the substrates were kept at room temperature while rotated at 5 rpm. The RF power and the Argon pressure in the chamber were maintained constant at 100W and

30 m Torr, respectively. The deposition parameters are given in Table 1.

2.2 Diode fabrication

For MS junction diode fabrication, ZnSe coated Si substrates were loaded into the evaporation system. Firstly, when base pressure reached the value of 133×10^{-6} Pa, aluminum (Al) metal evaporated at 200 nm thickness on the back side of the Si. Then, the samples were placed into a rapid thermal annealing system for 1 min under 5×10^{-5} mbar at 300 °C for forming low resistivity ohmic back contact. Secondly, to fabricate the Schottky diodes, Au, Ag, and Al metal top contacts were deposited under base pressure 266×10^{-6} Pa using the thermal evaporation technique. The parameters used in the fabrication process of the diodes are given in Table 2. The evaporated metals formed circular dots of 0.675 μm in radius on the top of the substrates using a shadow mask technique. The designs of all contacts are shown in Fig. 1, and the images of the contacts are given in Fig. 2.

2.3 Characterization

The films' thicknesses were verified using a stylus profilometer (Veeco-Dektak 150). X-ray diffraction measurements were carried out using a Bruker D8 Advance with Cu-K_α ($\lambda = 1.5418 \text{ \AA}$) radiation diffractometer. The composition of these films was examined with an Omicron X-ray photoelectron (XPS) device using a non-monochromatic Mg K_α excitation source ($h\nu = 1253.6 \text{ eV}$). To determine the thin films' crystallinity, the films' surface morphology was examined by using Atomic Force Microscope (NanoMagnetics Instruments Ltd., Oxford, UK), in dynamic mode. To examine the electrical characterization of the device, (I–V) current–voltage characteristic was measured with the help of a Keithley 4200 semiconductor parameter analyzer by two probe technique at room temperature. All processes performed throughout the study are shown in Fig. 3 as a flowchart.

Table 1 Deposition parameters

Thickness(nm)	Deposition Time(min)	RF Power(W)	P _{base} (Pa × 10 ⁻⁶)
100	11	100	133
300	33	100	133
600	55	100	133

Table 2 Contact evaporation parameters

Parameters	Au	Ag	Al
P_{base} (Pa)	266×10^{-6}	266×10^{-6}	266×10^{-6}
$P_{\text{deposition}}$ (Pa)	133×10^{-6}	133×10^{-6}	133×10^{-6}
Substrate Rotation Speed (rpm)	5	5	5
Substrate Temperature (°C)	Room temperature	Room temperature	Room temperature
Deposition Power (W)	280W	250W	230W
Thickness (nm)	200	200	200

Fig. 1 Schematic structures of Schottky contact **a** Au, **b** Ag, and **c** Al

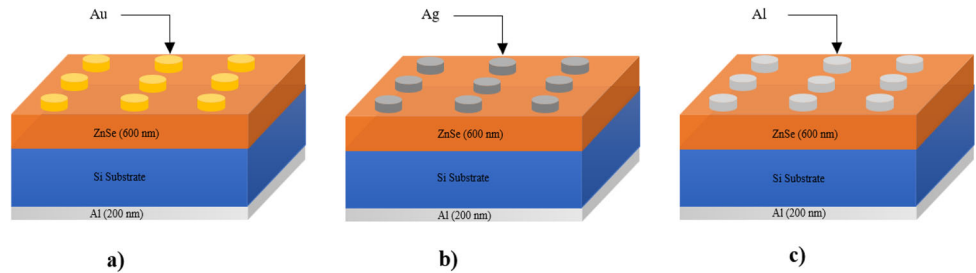


Fig. 2 Pictures of produced **a** Au, **b** Ag, and **c** Al contacts

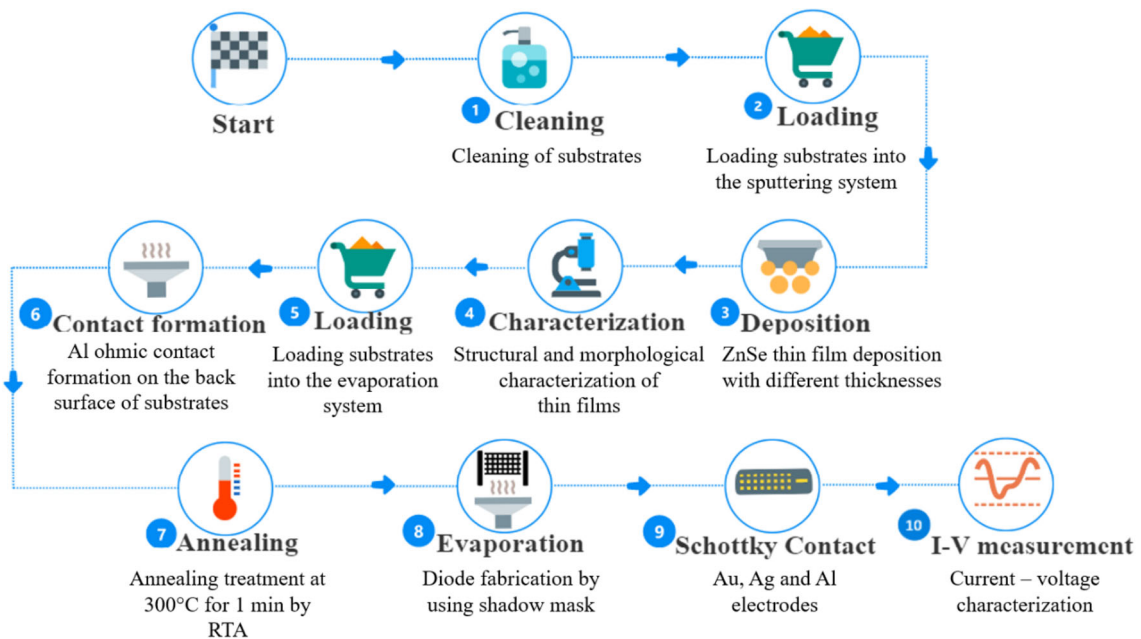
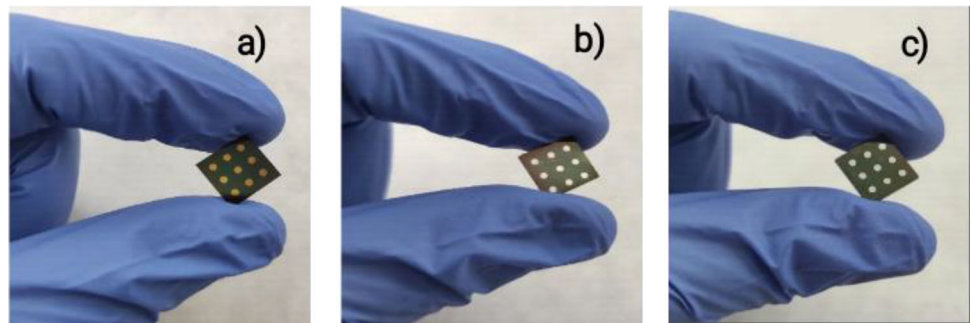


Fig. 3 Flowchart of the experimental procedure

3 Result and discussion

3.1 Structural and morphological characterization

3.1.1 XRD analysis

Structural characterization of the films produced was performed by using XRD. In Fig. 4, the results from XRD measurements were shown for ZnSe samples with three different thicknesses. ZnSe cubic structure (JPDS Card No. 01-081-8293) could be observed in the XRD patterns; the most prominent peaks are in the (111) orientation. The peak with high intensity corresponding to the (111) miller plane became stronger and sharper with increasing film thicknesses. Therefore, (111) orientation is the dominant crystal plane for all ZnSe produced films.

In order to examine the effect of the film thickness difference on the structural properties of ZnSe thin films in more detail, the strain was calculated together with the crystal structure parameters, such as grain size and lattice constant, using XRD data. The computed results are summarized in Table 3. It was observed that the ZnSe thin films were in the polycrystalline structure, and the crystallinity increased as the film thickness increased. The literature has confirmed that the crystallinity increases with an increment of film thickness [35, 36]. This increase in crystallinity could be attributed to increased aggregation, rearrangement of atoms, and decreased strain during film growth [34]. Structural parameters ZnSe film, including interplanar spacing of a material with a cubic crystal structure (d_{hkl}), the average grain size

of the film from the Debye-Scherrer formula (D), and strain on the film surface (ϵ_z) can be obtained by using Eqs. (1, 3), respectively.

$$d_{hkl} = \frac{a}{\sqrt{h^2 + k^2 + l^2}} \tag{1}$$

$$D = \frac{k\lambda}{\beta \cos \theta} \tag{2}$$

$$\epsilon_z = \frac{\Delta a}{a_0} = \frac{a_0 - a}{a_0} \tag{3}$$

where a is the lattice constant, a_0 is the reference lattice constant (theoretical value), k is a numerical factor called the crystallite-shape factor, with a value of about 0.94 for cubic systems, λ is the wavelength of the X-Ray, β is the Full Width Half Maximum (FWHM) and θ is the Bragg angle [37–40]. The growth orientation of the crystals affects the XRD peak intensity, while the position of the XRD peaks is affected by the grain size. Also, the FWHM values are inversely related to the crystallite size [41, 42]. As can be seen in Table 3, FWHM values decreased with increasing grain size for samples.

3.1.2 AFM analysis

The surface morphology of ZnSe thin films was analyzed by the AFM system. All measurements were made in a $3 \times 3 \mu\text{m}^2$ area and at room temperature. Two-dimensional (2D) topographic images of ZnSe thin films with three different film thicknesses are given in Fig. 5. As can be seen, the surface morphology of the films produced is homogeneous, and the particles have a regular shape and size.

The root mean square (RMS) values of the surface roughness obtained in the AFM measurement increased from 1.37 nm to 2.16 nm according to the increasing film thickness, and these values are given in Table 4. This indicates that the surface coating improves significantly as the film thickness increases. It was observed that the particle size increased due to the incrementation in crystallite agglomeration with the increase in film thickness [43, 44].

3.1.3 XPS analysis

X-ray photoelectron spectroscopy (XPS) is a powerful spectroscopy technique that is widely used in physics, chemistry, and especially in materials and chemical engineering to understand the surface

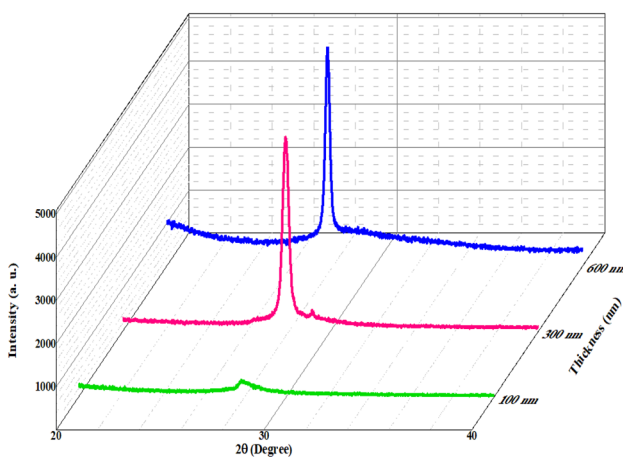
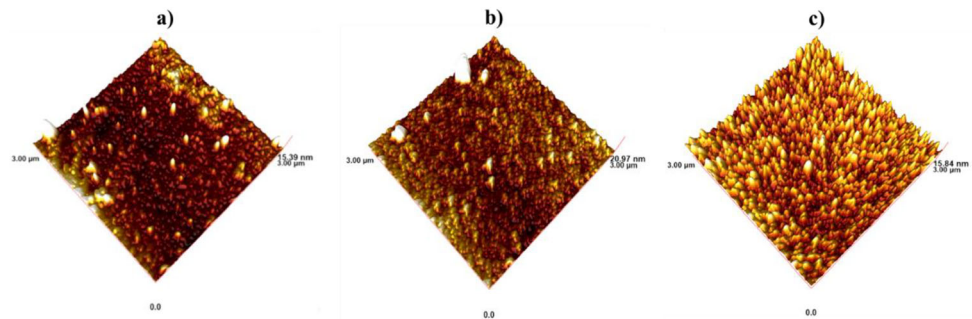


Fig. 4 XRD patterns of ZnSe films

Table 3 Parameters calculated from XRD patterns ZnSe thin films

Thickness (nm)	hkl	2θ ($^\circ$)	FWHM (nm)	Grain Size (nm)	Lattice Constant " α " (\AA)	Strain (ϵ_a)
100	[111]	27.857	0.768	11.14	5.5471	0.006188
300	[111]	27.844	0.342	25.01	5.5496	0.006035
600	[111]	27.318	0.247	34.63	5.5726	0.00162

Fig. 5 2D AFM images
a 100 nm b 300 nm c 600 nm**Table 4** RMS values of ZnSe thin films

Film Thickness (nm)	Grain Size (nm)	RMS (nm)
100	16	1.37
300	34	1.49
600	45	2.16

chemistry of a material, analyze binding structures, and examine the properties of surfaces and interfaces. In the XPS technique, the chemical environment in which an atom is located, and the properties of the bonds have an effect on the binding energies of electrons at the nuclear level [45, 46]. This situation causes changes in the bonding structure due to the effect of the material's surface treatment or deposition parameters. The binding energies determined by XPS spectroscopy can be compared with the values in the literature [47]. Accurate determination of binding energies in the XPS spectrum is possible by correctly calibrating the energy scale of the spectrometer.

Various conventional methods are available for calibrating binding energies [45], even if the material to be examined has low conductivity or poor contact structure properties, i.e., not a sufficient charge density. For example, the surface contamination layer's C1s peak, also known as the charge reference, uses so-called adventitious carbon (AdC). Thus, it can be presented as a binding energy reference. However, problems such as the binding energy referencing

technique involving the C1s peak, inconsistencies in the referencing methodology, the lack of a well-defined energy value of C1s, and the complex chemical structure of contamination types greatly reduce the reliability of chemical structure identification in XPS. To overcome this problem, groundbreaking and innovative studies have been carried out recently in the XPS literature by G. Greczynski and L. Hultman. These studies present a comprehensive referencing technique on various material systems, including metals, nitrides, carbides, borides, oxides, and oxynitrides [45, 48–55]. In order to eliminate the conventional and traditional status quo interpretation technique, especially in the calibration of the adventitious carbon's C1s peak, and to eliminate false spectral interpretations, we used the binding energy referencing process developed by L. Hultman, which analyzes the C1s peak of AdC extensively analytically [45].

The binding energy of the C–C/C–H peak of AdC varies depending on the sample work function (ϕ_{SA}) in which it is accumulated and is $E_B + \phi_{SA} = \text{constant}$. A constant value of $E_B + \phi_{SA}$ indicates that C1s do not change with the vacuum level [45]. This constant $E_B + \phi_{SA}$ value was determined as 289.58 ± 0.14 eV for various material systems exposed to air between 7 min and 10 months [28, 45, 53].

In light of this information, we calculated the binding energies of the C–C/C–H peak of AdC ($E_B^{C-C/C-H}$) based on the work function of ZnSe

(ϕ_{ZnSe}) in the reference process of XPS data, according to the following expression:

$$E_B^{C-C/C-H} = 289.58 - \phi_{ZnSe} \quad (4)$$

The work function of ZnSe is 4.501 eV [56]; thus the binding energy of the C–C/C–H peak of AdC for ZnSe was calculated as 285.08 eV. The C–C/C–H peak of AdC is set to this value, and all other nuclear levels, such as Zn 3d, Zn 2p, Se 3d, and Se 2p are calibrated accordingly. In this study, a detailed XPS analysis was carried out for the 600 nm thick ZnSe structure with a large grain size and good crystallite. The C1s peak of AdC and the contamination elements such as C and H for 600 nm thick ZnSe are given in Fig. 6.

Since the ZnSe material system was exposed to the air environment before XPS measurement, the shapes and relative intensity distributions of the O–C=O and C–C/C–H peaks vary. Similar changes were observed in the trends and shapes of C1s core level spectra in studies in the literature [28, 45, 52, 53]. The binding energy of the C–C/C–H peak is 285.08 eV, and this value can present variability in the literature

according to different material systems and work functions of the materials [28, 45].

To confirm the presence of the ZnSe phase grown on Si substrate, XPS contains three elements, Zinc (Zn), Selenium (Se), Carbon (C), in the binding energies range of 10 eV to 1050 eV. A detailed XPS peak modeling of Zn 3d, Zn 2p, Se 3d, and Se 2p core level spectra obtained from ZnSe films exposed to air at 700 nm thickness using a Shirley type background and Voigt function is given in Fig. 7.

Investigations regarding chemical composition and the presence of each element were made by analysis of XPS spectra for Zn, Se, and C. Calibration of the Zn 3d, Zn 2p, Se 3d, and Se 2p core levels was adjusted according to the C–C/C–H transition of the C1s peak of AdC. The core level spectra for Zn 2p_{1/2} and Zn 2p_{3/2} are 1041 eV and 1017.73 eV, respectively. The spin-orbit splitting for Zn 2p is 23.27 eV and is consistent with values in the literature

[57–60]. The core level for Zn 3p is 1.38 eV and is very close to the values observed in the literature [60].

Figures 7c, d show that when the Se 2p and Se 3d core level spectra are examined, the binding energies for Se 2p_{1/2} and Se 2p_{3/2} are 166.98 eV and 161.62 eV, respectively, and are very close to the values in the literature [60, 61]. In addition, the binding energy separation between the two peaks for Se 2p depends on the chemical state of the Se atoms, and the spin-orbit splitting value for Se 2p_{1/2} and Se 2p_{3/2} is 5.36 eV. The binding energies for Se 3d_{3/2} and Se 3d_{5/2} are 56.19 eV and 55.11 eV, respectively, and are consistent with the values observed in the literature [60–62].

For the determination of C and H contamination elements and Zn/Se stoichiometry, in examining the XPS spectra given in Fig. 6, it is possible to perform quantitative analysis by analyzing the peak at each energy level and fitting it to the experimental data without resorting to any software and manual. For a material system containing n elements, the molar concentration of any element i is given as x_i , A_i is the area of the relevant core-level peak, and s_i is the relative sensitivity factor (RSF) [28]:

$$x_i = \frac{\frac{A_i}{s_i}}{\sum_i^n \left(\frac{A_i}{s_i}\right)} \quad (5)$$

Atomic concentration values were calculated by determining the molar concentration for Zn and Se in the ZnSe material system. In Table 5, surface atomic concentrations and binding energies of core-level

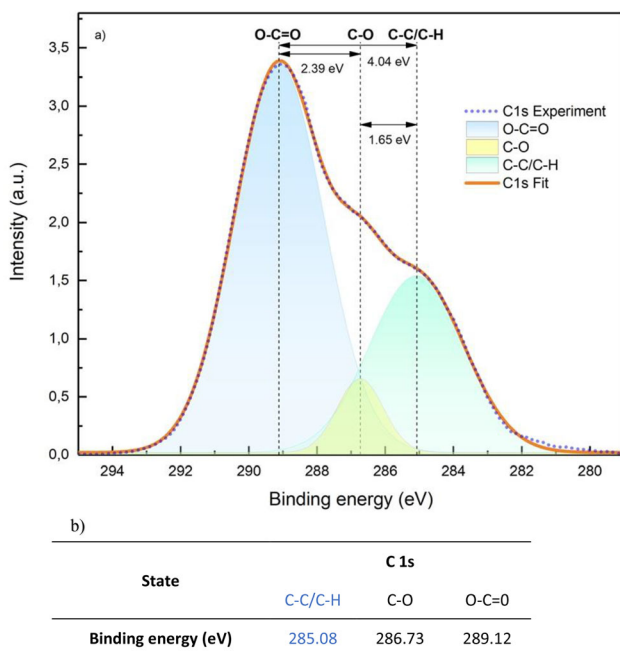


Fig. 6 a Detailed XPS peak modeling for the fitted C1s spectrum of ZnSe exposed to air at 600 nm thickness for more than one month using the Shirley-type background and Voigt functions. b Numerical values of O–C=O, C–O, and C–C/C–H levels containing contamination elements such as C and H

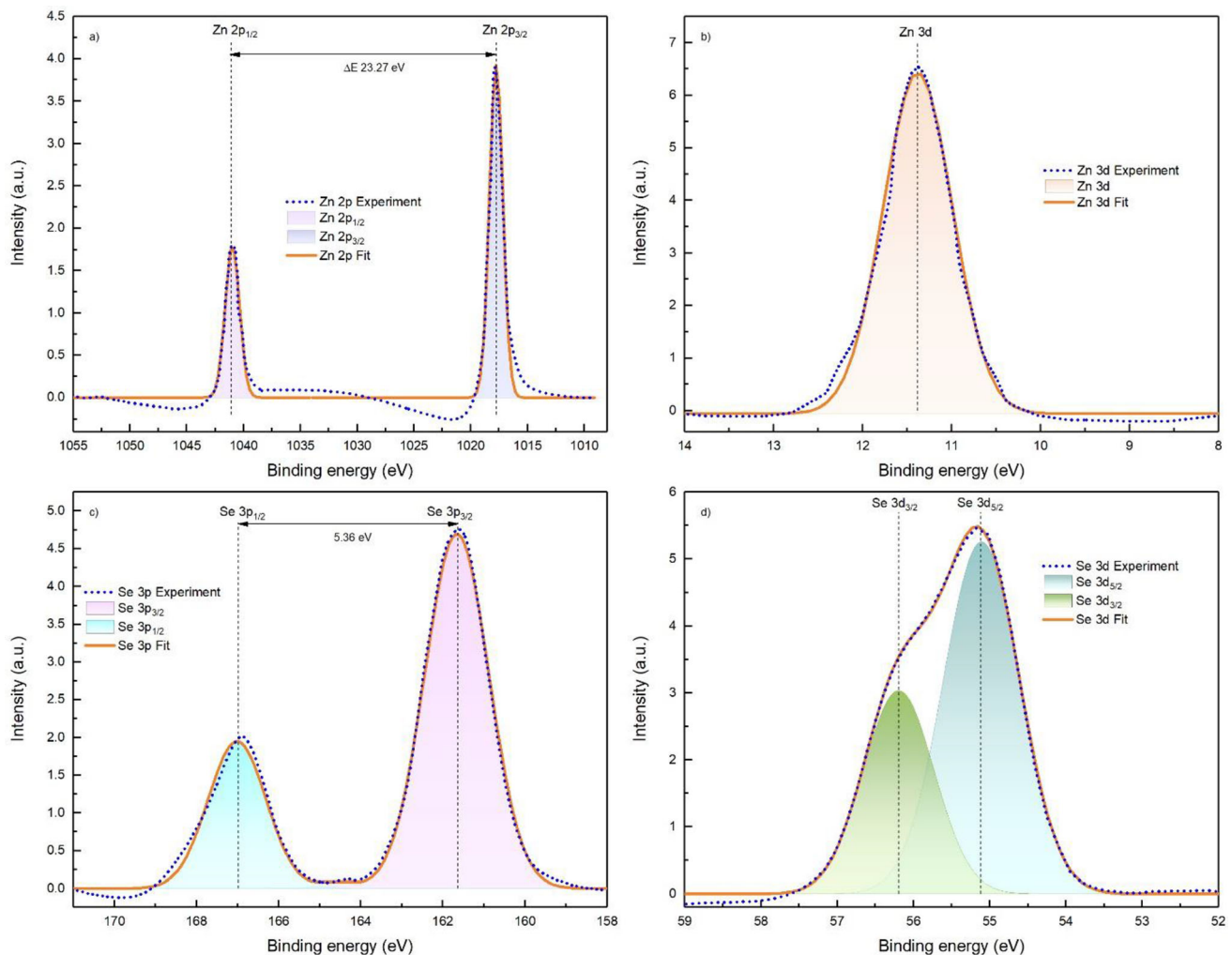


Fig. 7 Detailed XPS peak modeling of 600 nm thick ZnSe exposed to air for more than one month for **a** Zn 3d, **b** Zn 2p, **c** Se 3d, and **d** Se 2p core level spectra fitted using Shirley-type background and Voigt functions. The numerical value of each energy sink is given in Table 1

Table 5 Binding energies of core-level levels obtained from XPS spectra for ZnSe and surface atomic concentrations for determination of Zn/Se stoichiometry

State	Zn			Se				C 1 s		
	3d	2p _{3/2}	2p _{1/2}	3d _{5/2}	3d _{3/2}	2p _{3/2}	2p _{1/2}	C–C/C–H	C–O	O–C=O
Binding energy (eV)	11.38	1017.73	1041.00	55.11	56.19	161.62	166.98	285.08	286.73	289.12
Atomic concentration (%)	9.12	12.15	13.19	6.85	7.28	12.23	8.73	2.38	1.13	26.92
	34.46			35.10				30.44		

levels are given for determining Zn/Se stoichiometry obtained from XPS spectra for ZnSe. By analysis, the atomic percentages of Zn and Se elements for ZnSe were determined as 34.46% and 35.10%, respectively. With these percentages, it is understood that the Zn/Se stoichiometry is 0.98. The high carbon ratio is due

to the fact that ZnSe has been exposed to the atmosphere for a long time and the C contamination is quite high on its surface. In addition, a similar effect is seen in the literature with the contribution of the adhesive tape on which the sample is held [28].

3.2 Electrical characterization

In order to analyze whether the structure with 600 nm ZnSe layer whose structural and morphological characterization has been completed, which has the largest grain size, good crystallite, and low FWHM value, is suitable for an electronic device, the electrical characteristic at room temperature was examined. In this current work, a detailed I-V analysis of Metal/ZnSe/Si MIS structure obtained by using different metal contact layers (Au, Ag, and Al) was performed.

I-V measurements were performed for Au/ZnSe/Si, Ag/ZnSe/Si, and Al/ZnSe/Si MIS structures produced on ZnSe films on the 600 nm thickness, which have large grain size and crystal quality. The basic electrical parameters of the MIS structures were calculated using three different methods: TE, Cheung I-II, and Norde functions. The reason for choosing these methods is to obtain reliable and valid results and to be comparable to each other. Figure 8 shows the semi-logarithmic scale I-V curves of three different metal contacts. When these graphs were examined, it was clearly seen that the diodes produced were diodes with rectifier characters [63] (Fig. 9).

When the forward bias voltage was applied to the MIS structures, the thermionic emission theory explained current flow. Thermionic emission theory can be defined by,

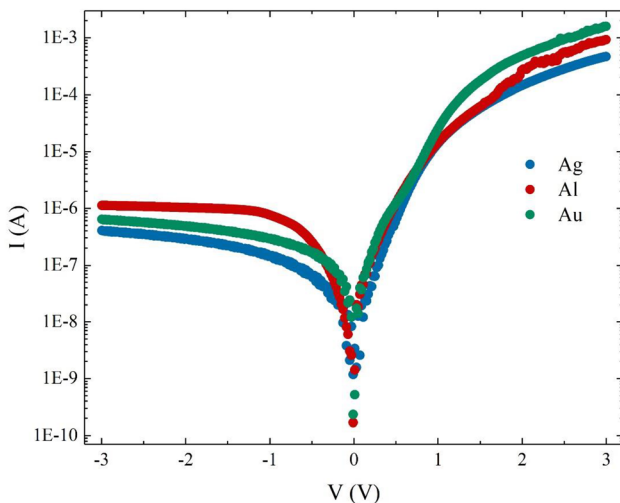


Fig. 8 The semi-logarithmic scale I-V curves of three different metal contacts

$$I = I_0 \left[\exp\left(\frac{e(V - IR_s)}{\eta kT}\right) - 1 \right] \tag{6}$$

where $V - IR_s$ is the voltage dropped across the series resistance (R_s) and I_0 is the saturation current expressed by [64].

$$I = AA^*T^2 \exp\left(\frac{-e\phi_b}{kT}\right) \tag{7}$$

The ideality factor (η) and the barrier height ϕ_b () can be expressed by Eqs. 8 and 9, respectively [65, 66];

$$\eta = \frac{e}{kT} \left(\frac{dV}{d(\ln I)} \right) \tag{8}$$

$$\phi_b = \frac{kT}{e} \ln \left[\frac{AA^*T^2}{I_0} \right] \tag{9}$$

where e , k , T , A , and A^* is the electric charge, the Boltzmann’s constant, temperature (K), contact area, and Richardson constant, respectively [67, 68]. Moreover, the significant electrical parameters such as η , R_s and ϕ_b can be calculated from the Cheung I-II functions, using the linearity in the region where the forward bias I-V graph begins to bend downward. Cheung I function can be defined as,

$$\frac{dV}{d(\ln I)} = \frac{\eta kT}{e} + IR_s \tag{10}$$

The current-dependent graph of the left side of the equation shows linearity and the slope of this linear region gives the series resistance (R_s), while the ideality factor (η) value is obtained from the intersection of the $\frac{dV}{d(\ln I)}$ axis [64]. Cheung II function can be defined as,

$$H(I) = V - \left(\frac{\eta kT}{e} \right) \ln \left[\frac{I}{AA^*T^2} \right] = \eta\phi_b + IR_s \tag{11}$$

A linear region is obtained when $H(I)$ is plotted against I . The series resistance (R_s) can be calculated from the slope of this linear region and the barrier height ϕ_b from the point where it intersects the vertical axis. Another way to calculate series resistance and barrier height is the Norde method. Norde function can be expressed as,

$$F(V) = \frac{V}{\gamma} - \frac{kT}{q} \ln \left(\frac{I(V)}{AA^*T^2} \right) \tag{12}$$

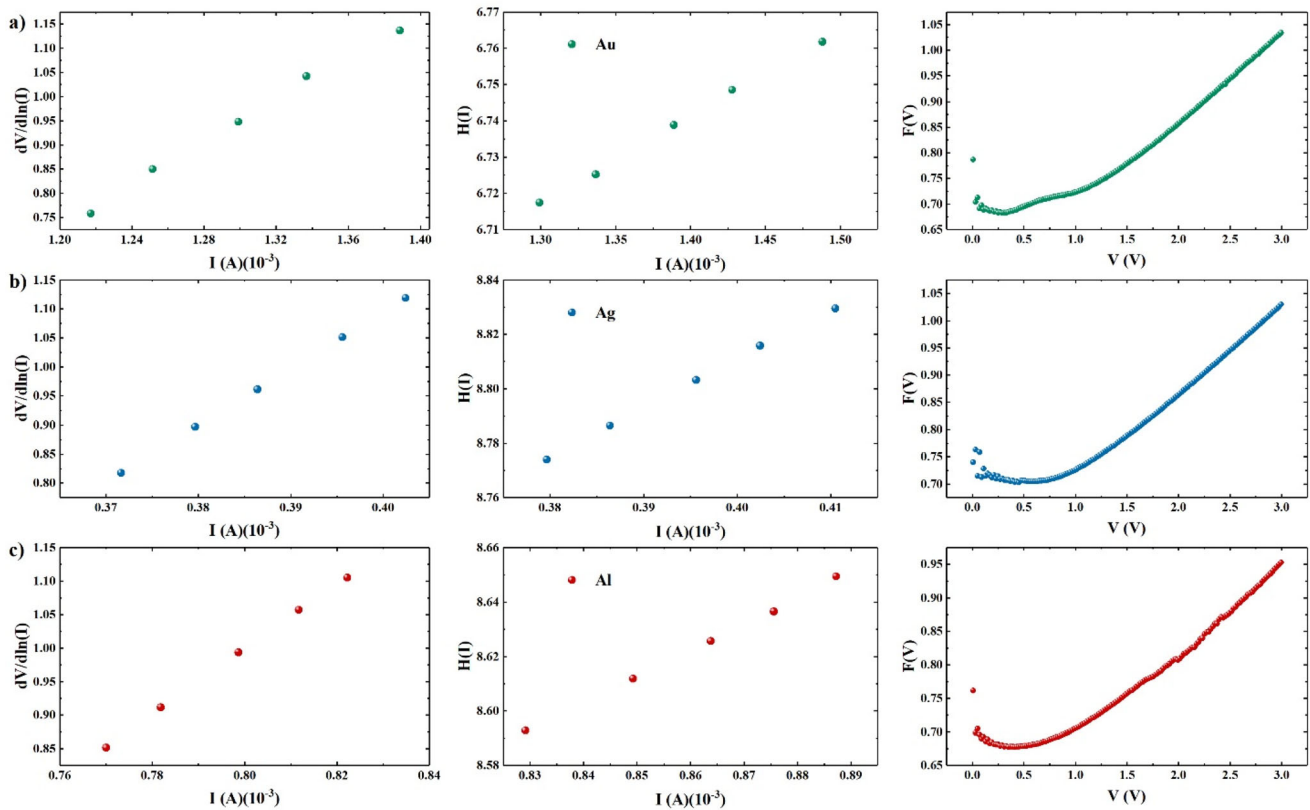


Fig. 9 Plot of $dV/d\ln(I)$ — I , $H(I)$ — I and $F(V)$ — V for **a** Au, **b** Ag, and **c** Al metal contact

$$\phi_b = F(V_0) + \frac{V_0}{\gamma} - \frac{kT}{q} \tag{13}$$

$$R_s = \frac{kT(\gamma - \eta)}{I} \tag{14}$$

γ is the smallest integer greater than the ideality factor, which is extracted from the $\ln(I)$ — V graph ϕ_b , and R_s can be obtained from the Eqs. (13, 14), respectively [69–71].

The electrical properties of the fabricated ZnSe thin films with different metal contacts were summarized in Table 6, which revealed that the MIS structure formed using Au metal showed better electrical performance compared to those formed using Al and Ag metals. The values of basic electrical parameters, including ideality factor, barrier height, and series resistance, were found to be significantly influenced by the choice of metal contact. The MIS structure formed with Au metal contact exhibited an ideality factor of 3.81 and a barrier height of 0.835 eV, which were in agreement with the findings of a study by Çakıcı et al. [38].

Table 6 Comparison of η , ϕ_{b0} and R_s values obtained by Thermionic Emission, Cheung I-II and Norde methods for three different metal contacts

Parameters	Method	Au contact	Ag contact	Al contact
η	lnI—V	3.81	4.10	4.68
	$dV/d\ln(I)$	7.67	11.24	11.76
	$F(V)$	0.718	0.766	0.725
$\phi_{b0}(eV)$	lnI—V	0.755	0.779	0.747
	H(I)	0.835	0.719	0.662
	H(I)	239	1803	967
$R_s(\Omega)$	lnI—V	1867	6346	3190
	$dV/d\ln(I)$	1865	9763	4878
	F(V)	7294	5349	3742

4 Conclusion

ZnSe thin films with three different thicknesses were deposited by the sputtering technique on Si substrates. As a result of the characterizations, MIS structures fabrication was performed ZnSe thin film with 600 nm thickness because of having high crystal

quality and uniform morphology. It was observed that the particle size increased from 11.14 to 34.63 nm with the increase of the film thickness, while the strain value decreased. These data also support that the increase in film thickness increases the crystallinity. The surface morphology measurements observed that the particle size increased from 16 to 45 nm as the film thickness increased. In addition, the AFM images prove that the film has a more homogeneous surface with the increase in thickness. With detailed analysis of XPS spectra, surface atomic concentrations and binding energies of core-level levels are determined for Zn/Se stoichiometry in ZnSe. The atomic percentages of Zn and Se elements for ZnSe were calculated and thus Zn/Se stoichiometry is obtained as 0.98. Then Au/ZnSe/Si, Ag/ZnSe/Si, and Al/ZnSe/Si MIS structures were fabricated and investigated. The electrical characterization shows that Au/ZnSe/Si Schottky diode with $\eta = 3,81$, $\phi_{b0} = 0,718$ eV and $R_s = 239 \Omega$ has better diode performance. The produced Au/ZnSe/Si MIS structure was determined as appropriate for optoelectronic applications.

Acknowledgements

This study was supported by the Directorate of the Presidential Strategy and Budget of Turkey (Project No: 2019K12-149045).

Author contributions

EB: Conceptualization, writing—original draft. BK: Investigation, writing—review and editing. ÇÇ: Conceptualization, Formal analysis. EÇ: Investigation, visualization. TA: Investigation, writing—original draft. NAS: Visualization, writing—review and editing. SS: Supervision. SÖ: Supervision.

Data availability

The datasets analyzed during the current study are available from the corresponding author on reasonable request.

Declarations

Conflict of interest The authors declare that there is no conflict of interest.

References

1. Md.A. Sayeed, H.K. Rouf, KMd.A. Hussain, Effect of thickness on characteristics of ZnSe thin film synthesized by vacuum thermal evaporation. *J. Theor. Appl. Phys.* **14**, 251–259 (2020). <https://doi.org/10.1007/s40094-020-00378-1>
2. S. Chuhadiya, R. Sharma, S.L. Himanshu, S. Patel, M.D. Chander, M.S.D. Kannan, Thermal annealing induced physical properties of ZnSe thin films for buffer layer in solar cells. *Phys. E Low Dimens. Syst. Nanostruct.* **117**, 113845 (2020). <https://doi.org/10.1016/j.physe.2019.113845>
3. K. Ou, S. Wang, L. Bai, Y. Wang, K. Zhang, L. Yi, Investigation on annealing temperature-dependent optical properties of electron beam evaporated ZnSe thin films. *Thin Solid Films* **669**, 247–252 (2019). <https://doi.org/10.1016/j.tsf.2018.11.013>
4. Md. Abu Sayeed, H.K. Rouf, Fabrication and Characterization of Zinc Selenide (ZnSe) Thin Film in Solar Cell Applications, in: 2018 International Conference on Innovations in Science, Engineering and Technology (ICISSET), IEEE, 2018: p. 247–250. <https://doi.org/10.1109/ICISSET.2018.8745544>
5. J. Sharma, H. Singh, T. Singh, A. Thakur, Structural, optical and photo-electrical properties of nanocrystalline ZnSe thin films. *J. Mater. Sci.: Mater. Electron.* **29**, 5688–5695 (2018). <https://doi.org/10.1007/s10854-018-8538-x>
6. K. Ou, S. Wang, X. Zhang, L. Yi, Novel blue-light-emitting diodes based on nanostructured ZnSe/ZnS multilayer films. *J. Mater. Sci.* **54**, 4049–4055 (2019). <https://doi.org/10.1007/s10853-018-3132-4>
7. Z. Nasiri, H. Fallah, M. Hajimahmoodzadeh, M. Mardiha, Investigation of the laser induced damage thresholds of all-dielectric and metal-dielectric mirrors for a continuous wave at 10.6 μm . *Opt Mater (Amst)*. **114**, 110936 (2021). <https://doi.org/10.1016/j.optmat.2021.110936>
8. W. Liu, D. Gu, X. Li, Ultrasensitive NO₂ detection utilizing mesoporous ZnSe/ZnO heterojunction-based chemiresistive-type sensors. *ACS Appl. Mater. Interfaces* **11**, 29029–29040 (2019). <https://doi.org/10.1021/acsami.9b07263>
9. G.K. Rao, Electrical and photoresponse properties of vacuum deposited Si/Al:ZnSe and Bi:ZnTe/Al:ZnSe photodiodes. *Appl. Phys. A* **123**, 224 (2017). <https://doi.org/10.1007/s00339-017-0850-4>
10. G. Feng, C. Yang, S. Zhou, Nanocrystalline Cr²⁺-doped ZnSe Nanowires Laser. *Nano Lett.* **13**, 272–275 (2013). <https://doi.org/10.1021/nl304066h>

11. T.R. Kumar, P. Prabukanthan, G. Harichandran, J. Theerthagiri, A.M. Moydeen, G. Durai, P. Kuppusami, T. Tatarchuk, Comparative study of structural, optical and electrical properties of electrochemically deposited Eu, Sm and Gd doped ZnSe thin films. *J. Mater. Sci.: Mater. Electron.* **29**, 5638–5648 (2018). <https://doi.org/10.1007/s10854-018-8533-2>
12. V.F. Kobziev, R.M. Zakirova, N.V. Kostenkov, P.N. Krylov, I.V. Fedotova, Effect of deposition temperature on the structure and optical properties of zinc-selenide films produced by radio-frequency magnetron sputtering. *Semiconductors.* **51**, 817–822 (2017). <https://doi.org/10.1134/S1063782617060161>
13. S.A. Rodin, E.M. Gavrishchuk, V.B. Ikonnikov, D.V. Savin, Effect of annealing atmosphere on chromium diffusion in CVD ZnSe. *Inorg. Mater.* **54**, 21–25 (2018). <https://doi.org/10.1134/S0020168518010132>
14. N. Mavridi, J. Zhu, N.M. Eldose, K.A. Prior, R.T. Moug, Adhesion measurements of epitaxially lifted MBE-Grown ZnSe. *J. Electron. Mater.* **47**, 4394–4398 (2018). <https://doi.org/10.1007/s11664-018-6372-9>
15. D.-X. Qing, S.-T. Wang, S.-G. Ning, W. Zhang, X.-X. Chen, H. Zhang, G.-Y. Feng, S.-H. Zhou, Influences of annealing temperature on properties of Fe²⁺:ZnSe thin films deposited by electron beam evaporation and their applications to Q-switched fiber laser*. *Chin. Phys. B.* **29**, 054208 (2020). <https://doi.org/10.1088/1674-1056/ab81f2>
16. M.G. Mahesha, N. Rashmitha, M. Meghana, Padiyar, Investigation of effect of annealing on thermally evaporated ZnSe thin films through spectroscopic techniques. *Phys. B Condens. Matter* **520**, 37–42 (2017). <https://doi.org/10.1016/j.physb.2017.06.011>
17. V.B. Shrotriya, J. Singh, D. Bhardwajc, Growth of ZnSe Thin Films by Sol-Gel Method, 2020.
18. J.P.B. Silva, K.C. Sekhar, R.F. Negrea, C. Ghica, D. Dastan, M.J.M. Gomes, Ferroelectric properties of ZrO₂ films deposited on ITO-coated glass. *Ceram. Int.* **48**, 6131–6137 (2022). <https://doi.org/10.1016/j.ceramint.2021.11.152>
19. M.K.A. Mohammed, A.K. Al-Mousoi, S. Singh, U. Younis, A. Kumar, D. Dastan, G. Ravi, Ionic liquid passivator for mesoporous titanium dioxide electron transport layer to enhance the efficiency and stability of hole conductor-free perovskite solar cells. *Energy Fuels* **36**, 12192–12200 (2022). <https://doi.org/10.1021/acs.energyfuels.2c01980>
20. S. Talu, S. Kulesza, M. Bramowicz, K. Stepień, D. Dastan, Analysis of the surface microtexture of sputtered indium tin oxide thin films. *Arch. Metall. Mater.* **66**, 443–450 (2021). <https://doi.org/10.24425/amm.2021.135877>
21. D. Dastan, K. Shan, A. Jafari, F. Gity, X.T. Yin, Z. Shi, N.D. Alharbi, B.A. Reshi, W. Fu, Ş. Tâlu, L. Aljerf, H. Garmestani, L. Ansari, Influence of nitrogen concentration on electrical, mechanical, and structural properties of tantalum nitride thin films prepared via DC magnetron sputtering. *Appl Phys A Mater Sci Process.* **128**, 1–16 (2022). <https://doi.org/10.1007/s00339-022-05501-4>
22. O. Toma, V.-A. Antohe, A.-M. Panaitescu, S. Iftimie, A.-M. Răduță, A. Radu, L. Ion, Ş. Antohe, Effect of RF Power on the physical properties of sputtered ZnSe nanostructured thin films for photovoltaic applications. *Nanomaterials* **11**, 2841 (2021). <https://doi.org/10.3390/nano11112841>
23. L. Ion, S. Iftimie, A. Radu, V.A. Antohe, O. Toma, S. Antohe, Physical properties of RF-sputtered ZnSe thin films for photovoltaic applications: Influence of film thickness. *Porc. Rom. Acad. Ser. A.* **22**, 25–34 (2021)
24. A. Eroğlu, S. Demirezen, Y. Azizian-Kalendaragh, Ş. Altındal, A comparative study on the electrical properties and conduction mechanisms of Au/n-Si Schottky diodes with/without an organic interlayer. *J. Mater. Sci.: Mater. Electron.* **31**, 14466–14477 (2020). <https://doi.org/10.1007/s10854-020-04006-1>
25. A. Tataroğlu, Ş. Altındal, Y. Azizian-Kalendaragh, Electrical characterization of Au/n-Si (MS) diode with and without graphene-polyvinylpyrrolidone (Gr-PVP) interface layer. *J. Mater. Sci.: Mater. Electron.* **32**, 3451–3459 (2021). <https://doi.org/10.1007/s10854-020-05091-y>
26. B. Akin, J. Farazin, Y. Azizian-Kalendaragh, Altındal, A comparison electric-dielectric features of Al/p-Si (MS) and Al/(Al₂O₃:PVP)/p-Si (MPS) structures using voltage-current (V–I) and frequency-impedance (f–Z) measurements. *J. Mater. Sci.: Mater. Electron.* **33**, 21963–21975 (2022). <https://doi.org/10.1007/s10854-022-08984-2>
27. B. Kınacı, Ç. Çetinkaya, E. Çokduygular, H.İ. Efkere, N.A. Sönmez, S. Özçelik, Negative capacitance phenomena in Au/SrTiO₃/p-Si heterojunction structure. *J. Mater. Sci.: Mater. Electron.* **31**, 8718–8726 (2020). <https://doi.org/10.1007/s10854-020-03406-7>
28. F. Güzelçimen, B. Tanören, Ç. Çetinkaya, M.D. Kaya, H.İ. Efkere, Y. Özen, D. Bingöl, M. Sirkeci, B. Kınacı, M.B. Ünlü, S. Özçelik, The effect of thickness on surface structure of rf sputtered TiO₂ thin films by XPS, SEM/EDS, AFM and SAM. *Vacuum.* **182**, 109766 (2020). <https://doi.org/10.1016/j.vacuum.2020.109766>
29. B. Kınacı, E. Çelik, E. Çokduygular, Ç. Çetinkaya, Y. Yalçın, H.İ. Efkere, Y. Özen, N.A. Sönmez, S. Özçelik, Effect of annealing on the surface morphology and current-voltage characterization of a CZO structure prepared by RF magnetron sputtering. *Semiconductors* **55**, 28–36 (2021). <https://doi.org/10.1134/S1063782621010115>
30. C. Bairam, Y. Yalçın, H.İ. Efkere, E. Çokduygular, Ç. Çetinkaya, B. Kınacı, S. Özçelik, Structural, morphological, optical and electrical properties of the Ti doped-ZnO (TZO)

- thin film prepared by RF sputter technique. *Phys. B Condens. Matter.* **616**, 413126 (2021). <https://doi.org/10.1016/j.physb.2021.413126>
31. B. Kınacı, C. Bairam, Y. Yalçın, E. Çokduygular, Ç. Çetinkaya, H.İ Efkere, S. Özçelik, Evaluation of dielectric properties of Au/TZO/n–Si structure depending on frequency and voltage. *J. Mater. Sci.: Mater. Electron.* **33**, 10516–10523 (2022). <https://doi.org/10.1007/s10854-022-08038-7>
 32. B. Kınacı, Dielectric properties of Au/SrTiO₃/p-Si structure obtained by RF magnetron sputtering in a wide frequency range. *Silicon* **14**, 2717–2722 (2022). <https://doi.org/10.1007/s12633-021-01067-7>
 33. H.İ Efkere, A.E. Gümrükcü, Y. Özen, B. Kınacı, S.Ş Aydın, H. Ates, S. Özçelik, Investigation of the effect of annealing on the structural, morphological and optical properties of RF sputtered WO₃ nanostructure. *Phys. B Condens. Matter.* **622**, 413350 (2021). <https://doi.org/10.1016/j.physb.2021.413350>
 34. M.F. Hasaneen, Z.A. Alrowaili, W.S. Mohamed, Structure and optical properties of polycrystalline ZnSe thin films: validity of Swanepol's approach for calculating the optical parameters. *Mater. Res. Express* **7**, 016422 (2020). <https://doi.org/10.1088/2053-1591/ab6779>
 35. H.I. Elsaedy, A.A. Hassan, H.A. Yakout, A. Qasem, The significant role of ZnSe layer thickness in optimizing the performance of ZnSe/CdTe solar cell for optoelectronic applications. *Opt. Laser Technol.* **141**, 107139 (2021). <https://doi.org/10.1016/j.optlastec.2021.107139>
 36. T. Prasada Rao, M.C. Santhoshkumar, Effect of thickness on structural, optical and electrical properties of nanostructured ZnO thin films by spray pyrolysis. *Appl. Surf. Sci.* **255**, 4579–4584 (2009). <https://doi.org/10.1016/j.apsusc.2008.11.079>
 37. M.G. Norton, C. Suryanarayana, *X-Ray diffraction: a practical approach* (Plenum Press, Boston, 1998)
 38. B.D. Cullity, S.R. Stock, *Elements of X-ray Diffraction*, 3rd edn. (Pearson, United Kingdom, 2014).
 39. J.-M. Wagner, F. Bechstedt, Properties of strained wurtzite GaN and AlN: Ab initio studies. *Phys. Rev. B.* **66**, 115202 (2002). <https://doi.org/10.1103/PhysRevB.66.115202>
 40. M.K. Öztürk, H. Altuntaş, S. Çörekçi, Y. Hongbo, S. Özçelik, E. Özbay, Strain-stress analysis of AlGa_xN/GaN heterostructures with and without an AlN buffer and interlayer. *Strain* **47**, 19–27 (2011). <https://doi.org/10.1111/j.1475-1305.2009.00730.x>
 41. D. Dastan, Effect of preparation methods on the properties of titania nanoparticles: solvothermal versus sol–gel. *Appl. Phys. A Mater. Sci. Process.* **123**, 1–13 (2017). <https://doi.org/10.1007/s00339-017-1309-3>
 42. D. Dastan, K. Shan, A. Jafari, T. Marszalek, M.K.A. Mohammed, L. Tao, Z. Shi, Y. Chen, X.T. Yin, N.D. Alharbi, F. Gity, S. Asgary, M. Hatamvand, L. Ansari, Influence of heat treatment on H₂S gas sensing features of NiO thin films deposited via thermal evaporation technique. *Mater. Sci. Semicond. Process.* **154**, 107232 (2023). <https://doi.org/10.1016/j.mssp.2022.107232>
 43. G.I. Rusu, M. Diciu, C. Pirghie, E.M. Popa, Structural characterization and optical properties of ZnSe thin films. *Appl. Surf. Sci.* **253**, 9500–9505 (2007). <https://doi.org/10.1016/j.apsusc.2007.06.009>
 44. R. Khalfi, D. Talantikite-Touati, A. Tounsi, H. Merzouk, Effect of deposition time on structural and optical properties of ZnSe thin films grown by CBD method. *Opt Mater (Amst).* **106**, 109989 (2020). <https://doi.org/10.1016/j.optmat.2020.109989>
 45. G. Greczynski, L. Hultman, X-ray photoelectron spectroscopy: towards reliable binding energy referencing. *Prog. Mater. Sci.* **107**, 100591 (2020). <https://doi.org/10.1016/j.pmatsci.2019.100591>
 46. E. Sokolowski, C. Nordling, K. Siegbahn, Chemical shift effect in inner electronic levels of Cu due to oxidation. *Phys. Rev.* **110**, 776–776 (1958). <https://doi.org/10.1103/PhysRev.110.776>
 47. B.V. Crist, XPS in industry—Problems with binding energies in journals and binding energy databases. *J. Electron. Spectros. Relat. Phenom.* **231**, 75–87 (2019). <https://doi.org/10.1016/j.elspec.2018.02.005>
 48. J. Okabayashi, A. Kimura, O. Rader, T. Mizokawa, A. Fujimori, T. Hayashi, M. Tanaka, Core-level photoemission study of Ga(1–x)MnxAs. *Phys. Rev. B.* **58**, 4211–4214 (1998). <https://doi.org/10.1103/PhysRevB.58.R4211>
 49. G. Greczynski, L. Hultman, Self-consistent modelling of X-ray photoelectron spectra from air-exposed polycrystalline TiN thin films. *Appl. Surf. Sci.* **387**, 294–300 (2016). <https://doi.org/10.1016/j.apsusc.2016.06.012>
 50. G. Greczynski, I. Petrov, J.E. Greene, L. Hultman, Al capping layers for nondestructive x-ray photoelectron spectroscopy analyses of transition-metal nitride thin films. *J. Vac. Sci. Technol., A: Vac., Surf. Films* **33**, 05E101 (2015). <https://doi.org/10.1116/1.4916239>
 51. G. Greczynski, L. Hultman, In-situ observation of self-cleansing phenomena during ultra-high vacuum anneal of transition metal nitride thin films: prospects for non-destructive photoelectron spectroscopy. *Appl. Phys. Lett.* **109**, 211602 (2016). <https://doi.org/10.1063/1.4968803>
 52. G. Greczynski, L. Hultman, C 1s Peak of adventitious carbon aligns to the vacuum level: dire consequences for material's bonding assignment by photoelectron spectroscopy. *Chem-PhysChem* **18**, 1507–1512 (2017). <https://doi.org/10.1002/cphc.201700126>

53. G. Greczynski, L. Hultman, Reliable determination of chemical state in x-ray photoelectron spectroscopy based on sample-work-function referencing to adventitious carbon: Resolving the myth of apparent constant binding energy of the C 1s peak. *Appl. Surf. Sci.* **451**, 99–103 (2018). <https://doi.org/10.1016/j.apsusc.2018.04.226>
54. A. Khatibi, J. Sjölen, G. Greczynski, J. Jensen, P. Eklund, L. Hultman, Structural and mechanical properties of Cr–Al–O–N thin films grown by cathodic arc deposition. *Acta Mater.* **60**, 6494–6507 (2012). <https://doi.org/10.1016/j.actamat.2012.08.010>
55. G. Greczynski, S. Mráz, L. Hultman, J.M. Schneider, Unintentional carbide formation evidenced during high-vacuum magnetron sputtering of transition metal nitride thin films. *Appl. Surf. Sci.* **385**, 356–359 (2016). <https://doi.org/10.1016/j.apsusc.2016.05.129>
56. A.F. Qasrawi, M.F. Taleb, Enhancement of electrical performance of ZnSe thin films via Au nanosandwiching. *Mater. Sci.-Pol.* **38**, 174–180 (2020). <https://doi.org/10.2478/msp-2020-0009>
57. Y.-C. Liang, C.-C. Wang, Surface crystal feature-dependent photoactivity of ZnO–ZnS composite rods via hydrothermal sulfidation. *RSC Adv.* **8**, 5063–5070 (2018). <https://doi.org/10.1039/C7RA13061A>
58. Y.I. Choi, S. Lee, S.K. Kim, Y.-I. Kim, D.W. Cho, M.M. Khan, Y. Sohn, Fabrication of ZnO, ZnS, Ag–ZnS, and Au–ZnS microspheres for photocatalytic activities, CO oxidation and 2-hydroxyterephthalic acid synthesis. *J. Alloys Compd.* **675**, 46–56 (2016). <https://doi.org/10.1016/j.jallcom.2016.03.070>
59. Z. Li, H. Chen, W. Liu, Full-spectrum photocatalytic activity of ZnO/CuO/ZnFe₂O₄ nanocomposite as a photofenton-like catalyst. *Catalysts* **8**, 557 (2018). <https://doi.org/10.3390/cata8110557>
60. J.R. Shallenberger, N. Hellgren, Zinc selenide analyzed by XPS. *Surf. Sci. Spectra* **27**, 014020 (2020). <https://doi.org/10.1116/6.0000165>
61. S. Hussain, K. Akbar, D. Vikraman, H. Liu, S.H. Chun, J. Jung, WS₂/CoSe₂ heterostructure: A designed structure as catalysts for enhanced hydrogen evolution performance. *J. Ind. Eng. Chem.* **65**, 167–174 (2018). <https://doi.org/10.1016/j.jiec.2018.04.025>
62. H. Liu, S. Hussain, A. Ali, B.A. Naqvi, D. Vikraman, W. Jeong, W. Song, K.-S. An, J. Jung, A vertical WSe₂–MoSe₂ p–n heterostructure with tunable gate rectification. *RSC Adv.* **8**, 25514–25518 (2018). <https://doi.org/10.1039/C8RA03398F>
63. T. Çakıcı, M. Özdal, M. Kundakçı, R. Kayalı, ZnSe and CuSe NP's by microbial green synthesis method and comparison of I–V characteristics of Au/ZnSe/p–Si/Al and Au/CuSe/p–Si/Al structures. *Mater. Sci. Semicond. Process.* **103**, 104610 (2019). <https://doi.org/10.1016/j.mssp.2019.104610>
64. S.K. Cheung, N.W. Cheung, Extraction of Schottky diode parameters from forward current-voltage characteristics. *Appl. Phys. Lett.* **49**, 85–87 (1986). <https://doi.org/10.1063/1.97359>
65. S.M. Sze, *Physics of Semiconductor Devices*, 2nd edn. (John Wiley and Sons, New Jersey, 1981)
66. H.C. Card, E.H. Rhoderick, Studies of tunnel MOS diodes I interface effects in silicon Schottky diodes. *J. Phys. D Appl. Phys.* **4**, 319 (1971). <https://doi.org/10.1088/0022-3727/4/10/319>
67. S. Alialy, Ş Altındal, E.E. Tanrıku, D.E. Yıldız, Analysis of temperature dependent current-conduction mechanisms in Au/TiO₂/n–4H–SiC (metal/insulator/semiconductor) type Schottky barrier diodes. *J. Appl. Phys.* **116**, 083709 (2014). <https://doi.org/10.1063/1.4893970>
68. D. Dastan, A. Banpurkar, Solution processable sol–gel derived titania gate dielectric for organic field effect transistors. *J. Mater. Sci.: Mater. Electron.* **28**, 3851–3859 (2017). <https://doi.org/10.1007/s10854-016-5997-9>
69. H. Norde, A modified forward I–V plot for Schottky diodes with high series resistance. *J. Appl. Phys.* **50**, 5052–5053 (1979). <https://doi.org/10.1063/1.325607>
70. Y. Azizian-Kalandaragh, J. Farazin, Ş Altındal, M. Shahedi Asl, G. Pirgholi-Givi, S.A. Delbari, A. Sabahi Namini, Electrical and dielectric properties of Al/(PVP: Zn–TeO₂)/p–Si heterojunction structures using current–voltage (I–V) and impedance–frequency (Z–f) measurements. *Appl. Phys. A.* **126**, 635 (2020). <https://doi.org/10.1007/s00339-020-03804-y>
71. B. Kınacı, S. Şebnem Çetin, A. Bengi, S. Özçelik, The temperature dependent analysis of Au/TiO₂ (rutile)/n–Si (MIS) SBDs using current–voltage–temperature (I–V–T) characteristics. *Mater. Sci. Semicond. Process.* **15**, 531–535 (2012). <https://doi.org/10.1016/j.mssp.2012.04.002>

Publisher's Note Springer Nature remains neutral with regard to jurisdictional claims in published maps and institutional affiliations.

Springer Nature or its licensor (e.g. a society or other partner) holds exclusive rights to this article under a publishing agreement with the author(s) or other rightsholder(s); author self-archiving of the accepted manuscript version of this article is solely governed by the terms of such publishing agreement and applicable law.